CHINESE OPTICS LETTERS

Vol. 19, No. 7 | July 2021

Passive devices at 2 μm wavelength on 200 mm CMOS-compatible silicon photonics platform [Invited]

Hui Ma (马 辉)[1], Haotian Yang (杨浩天)[1], Bo Tang (唐 波)[2], Maoliang Wei (魏茂良)[1], Junying Li (李钧颖)[1], Jianghong Wu (吴江宏)[3,4], Peng Zhang (张 鹏)[2], Chunlei Sun (孙春雷)[3,4], Lan Li (李 兰)[3,4], and Hongtao Lin (林宏焘)[1*]

[1] State Key Laboratory of Modern Optical Instrumentation, College of Information Science and Electronic Engineering, Zhejiang University, Hangzhou 310007, China

[2] Institute of Microelectronics, Chinese Academic Society, Beijing 100029, China

[3] Key Laboratory of 3D Micro/Nano Fabrication and Characterization of Zhejiang Province, School of Engineering, Westlake University, Hangzhou 310007, China

[4] Institute of Advanced Technology, Westlake Institute for Advanced Study, Hangzhou 310023, China

*Corresponding author: hometown@zju.edu.cn

Received April 12, 2021 | Accepted May 21, 2021 | Posted Online July 13, 2021

As a promising spectral window for optical communication and sensing, it is of great significance to realize on-chip devices at the 2 μm waveband. The development of the 2 μm silicon photonic platform mainly depends on the performance of passive devices. In this work, the passive devices were fabricated in the silicon photonic multi-project wafer process. The designed micro-ring resonator with a 0.6 μm wide silicon ridge waveguide based on a 220 nm silicon-on-insulator platform achieves a high intrinsic quality factor of 3.0×10^5. The propagation loss is calculated as 1.62 dB/cm. In addition, the waveguide crossing, multimode interferometer, and Mach–Zehnder interferometer were demonstrated at 2 μm with good performances.

Keywords: silicon photonics; integrated photonics; grating coupler; multimode interferometer; waveguide crossing.
DOI: 10.3788/COL202119.071301

1. Introduction

With the development of information technology, the channel capacity of current communication systems based on telecom-wavelength bands is gradually approaching their theoretical limits. The development of new technology will be the key to meeting the increasing demand for high-speed data transmission. Due to the recent advancement of the low-loss hollow-core photonic bandgap fiber[1] and large-bandwidth thulium-doped fiber amplifier (TDFA)[2], the 2 μm wavelength band is becoming an emerging communication window[3]. Besides, it is also emerging as a promising spectral window for chemical sensing, since the molecular fingerprint regions of many gases (e.g., CO_2, H_2O, and CH_4)[4] and the absorption bands of biomolecules like blood glucose fall in this wavelength range[5]. Thus, arguably, the 2 μm waveband has shown great potential in next-generation optical communication and sensing.

Complementary metal-oxide-semiconductor (CMOS)-compatible silicon photonic technology offers unique advantages for integrated devices at 2 μm in terms of high performance, large-scale fabrication, and low cost. Recently, some critical devices for this band, including lasers[6,7], modulators[8,9], photodetectors[10], on-chip spectrometers[11], and nonlinear optical devices[12,13], have been demonstrated on the silicon-on-insulator (SOI) platform. Meanwhile, as essential components of the on-chip photonic system[14], passive devices with different functions operating in the 2 μm band have also been demonstrated, including the low-loss single-mode waveguide[15], grating coupler (GC)[15,16], micro-ring resonator (MRR)[17], multimode interferometer (MMI)[18], arrayed waveguide grating[19], and mode demultiplexer[20,21]. Despite the significant progress that promotes the development and practical implementation of silicon photonics at the 2 μm waveband, some essential components, such as waveguide crossings, are still missing. Low-loss passive photonic components are the basis of high-performance optical communication and sensing systems.

In this paper, passive photonic devices operating at 2 μm were fabricated by using the silicon photonic multi-project wafer (MPW) process. A propagation loss of 1.62 dB/cm for ridge waveguides was calculated from MRRs with an intrinsic quality factor around 3.0×10^5. Waveguide crossing at 2 μm was designed and measured for the first time, to the best of our knowledge, with an insertion loss of less than 0.08 dB/crossing,

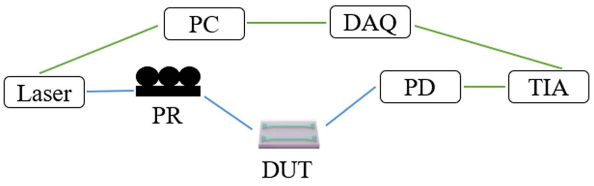

Fig. 1. Schematic diagram of the measurement system. PR, polarization rotator; DUT, device-under-test; PD, photodetector; TIA, trans-impedance amplifier; DAQ, data acquisition card; PC, personal computer.

and the coupling loss of the GC is optimized to be 7.9 dB/facet. Other passive devices, including the MMI and Mach–Zehnder interferometer (MZI), have been simultaneously designed, fabricated, and characterized at 2 μm.

2. Fabrication and Measurement System

The passive devices were fabricated with the 180 nm silicon photonic MPW process in the Institute of Microelectronics of Chinese Academy of Sciences (IMECAS). The ridge waveguide was etched by 150 nm and cladded by SiO_2 with 1 μm thickness. To characterize the fabricated 2 μm passive devices, we set up the measurement system shown in Fig. 1. A tunable laser (New Focus TLB-6700) was used as the light source. The light launched from the tunable laser was adjusted by the polarization rotator (PR) and coupled into the chip through a vertical coupling system. The transmission responses from the device-under-test (DUT) were monitored by an InGaAs PIN photodetector. The photocurrent from the diode was converted into a voltage signal through a trans-impedance amplifier (TIA) (Thorlabs PDA200 C) and then collected by a National Instruments (NI) data acquisition card (NI USB-6212). By sweeping the wavelength of the light source, high-resolution transmission spectra of the fabricated passive devices could be obtained.

3. SOI Passive Devices

3.1. Waveguide and micro-ring resonator

The cross section of the waveguide is shown in Fig. 2(a). To determine the single-mode condition and avoid high-order modes, we simulated the effective refractive index n_{eff} of the supported modes in the waveguides with different widths by finite differential element (FDE) simulation, as shown in Fig. 2(b). The designed waveguide was etched by 150 nm on a 220 nm silicon film, and the modal profile was shown in the inset of Fig. 2(b). A second-order mode appeared when the waveguide width is larger than 0.6 μm, as shown in the red effective index curve. To achieve better confinement while maintaining the single-mode condition, we chose the waveguide width as 0.6 μm.

MRRs were implemented to characterize the propagation loss of the waveguide. The inset in Fig. 3(a) is the SEM image of the MRR with a diameter of 80 μm. Transmission spectra of MRRs without and with light *p*-type doping are shown in

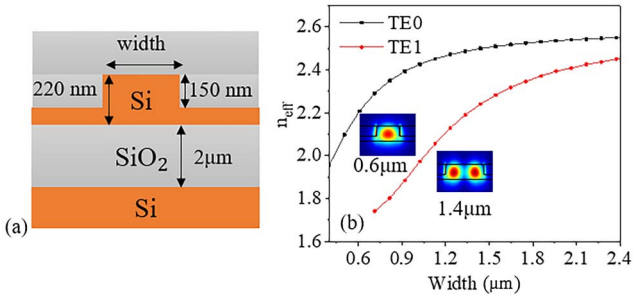

Fig. 2. (a) Cross-section diagram of the SOI ridge waveguide. (b) Calculated effective refractive index of the fundamental (black) and first-order (red) TE modes as a function of the ridge waveguide width at 2025 nm. Inset: the spatial distribution of the fundamental and second-order polarized optical modes into the SOI ridge waveguide with a width of 0.6 μm and 1.4 μm at 2025 nm, respectively.

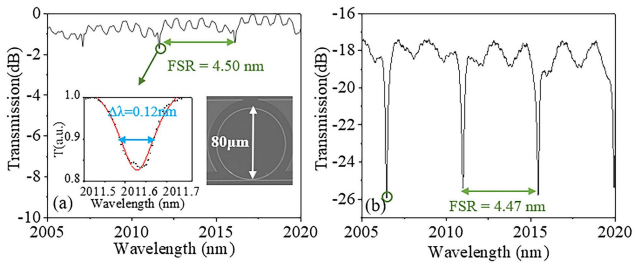

Fig. 3. (a) Measured spectral response of an MRR without doping. Inset: enlarged view of the measured resonance peak obtained by Lorentzian fitting and top-view SEM image of the MRR. (b) The measured spectral response of an MRR with light *p*-type doping.

Figs. 3(a) and 3(b), respectively. The gap between the coupling waveguide and the ring resonators of the two types of rings is 400 nm, and their extinction ratios are different due to the different propagation losses. Both rings were operated in the under-coupling regime, and their free spectral range (FSR) is about 4.5 nm. The corresponding group index is 3.58, which agrees well with our finite element simulation. Transmission spectra were fitted by using the coupled-mode theory[22]. The loaded quality factor (Q_{load}) of the MRR without doping is 1.7×10^4. The inferred propagation loss of the ring waveguide is about 1.62 dB/cm, and its intrinsic quality factor (Q_{in}) is as high as 3×10^5. On the other hand, the Q_{load} and Q_{in} of the MRR with light *p*-type doping (boron ion implantation with a doping concentration of $7 \times 10^{17}\,cm^{-3}$) are 1.1×10^4 and 3.5×10^4, respectively, and the inferred propagation loss is 13.7 dB/cm. The *p*-type doping in the MRR could have led to this excess loss. The low-loss ridge waveguide supports the applications in the 2 μm waveband.

3.2. Grating coupler

Due to the compact footprint and the convenience of alignment, GCs attracted extensive attention in fiber-to-waveguide couplings. Here, we designed and fabricated a 150 nm etched GC

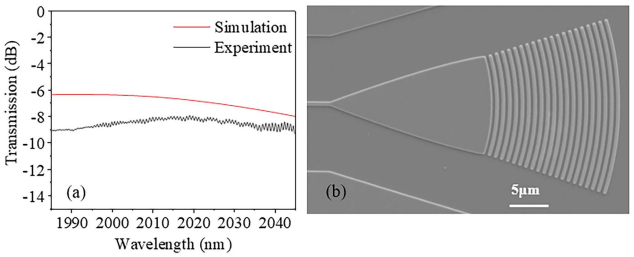

Fig. 4. (a) Simulated and measured coupling efficiency of the grating coupler. (b) Top-view SEM image of the fabricated GC.

(period 0.985 μm, duty cycle 0.5) with a coupling angle of 8 deg. Based on the Bragg equation, the period of the GC is estimated as below:

$$\Lambda = \frac{\lambda}{n_{\text{eff}} - n_1 \sin\theta}, \tag{1}$$

where Λ is the grating period, λ is the central wavelength, n_{eff} is the effective refractive index of the waveguide, n_1 is the index of cladding, and θ is the incident angle. The GC's optimized constant duty cycle was obtained by monitoring its coupling coefficiency in 3D finite difference time domain (FDTD) simulation while sweeping the grating period around the initial estimated value. The highest coupling efficiency is −6 dB for a grating period of 0.985 μm. As shown in Figure 4(a), the fabricated GC presents a minimal coupling loss of 7.9 dB at 2020 nm. The etching depth offset in the grating may have mainly resulted in the difference between the simulated and measured coupling efficiency.

3.3. Waveguide crossing

Waveguide crossings are basic components for large-scale on-chip optical interconnection. According to the self-imaging theory, many high-performance crossings have been demonstrated in communication wavebands[23–25]. We designed and fabricated the crossing operated at 2 μm with low insertion loss and crosstalk for the first time, to the best of our knowledge. The crossing is composed of two orthogonal 1 × 1 MMIs with a total size of 18.08 μm × 18.08 μm (length × width), and the main sizes of l_1, l_2, and w_1 are 3.5 μm, 11.08 μm, and 2.36 μm, which are shown in Fig. 5(b-3). The transmission spectra and spatial mode field distribution are shown in Fig. 5(a). By optimizing the taper region's width and length, the light beam is focused at the intersection region with a small amount of light leakage to the cross ports. To accurately characterize the insertion loss of waveguide crossings, cut-back measurement was performed via cascading 15, 30, and 45 waveguide crossings, as shown in Fig. 5(b-1). The zoom-in view of crossing is shown in Fig. 5(b-3). We fitted the transmission loss of these cascaded structures, as shown in Fig. 5(c), and achieved an insertion loss of 0.08 ± 0.011 dB for a single waveguide crossing. Based on the device structure shown in Fig. 5(b-2), the transmission spectra were measured from port 1 to ports 2 and 3, as depicted in Fig. 5(d). The crosstalk of the crossing is less than −34 dB.

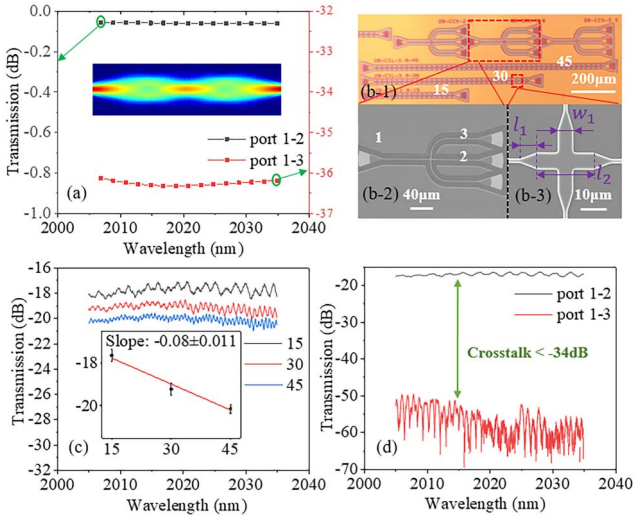

Fig. 5. (a) Simulated transmission spectra of the crossing from port 1 to ports 2 and 3 [the port numbers are shown in (b-2)]. Inset: electric field distribution at 2025 nm. (b) Microscope and SEM images of the cascaded and single crossing. (b-1) Microscope view of cascaded crossing with numbers 15, 30, and 45, and the device structure for crosstalk test; (b-2) enlarged view of the structure for crosstalk test; (b-3) enlarged view of a single crossing. (c) Cut-back measurements for characterizing the insertion loss of crossings. (d) Measurements of the device crosstalk.

3.4. Multimode interferometer

In the on-chip photonic system, MMI is one of the fundamental components for optical signal splitting and combining. Here, 1 × 2 MMIs were fabricated and characterized. Based on the self-imaging theory, the width and length of the MMIs were tuned to achieve a small footprint while maintaining low crosstalk between the two output waveguides. The 3D FDTD simulations were applied for the optimization. Here, we designed a 1 × 2 MMI with the total size of 72.5 μm × 4.4 μm (length × width) and main sizes of l_1, w_1, w_2, w_3, and taper lengths were 12.5 μm, 1.9 μm, 4.4 μm, 1.1 μm, and 30 μm, which are shown in Fig. 6(b-2). The designed insertion loss was −3.05 dB, and its transmission spectrum is shown in Fig. 6(a). To characterize the insertion loss of the designed MMI, a cascade structure shown in Fig. 6(b-1) was fabricated through the same MPW run. We measured the transmission spectra from port 0 to ports 1–7 [the number of ports is shown in Fig. 6(b-1)] of cascaded 1 × 2 MMIs in the 2005–2035 nm wavelength range, as depicted in Fig. 6(c). A linear fit of the transmission yields an insertion loss of −3.03 ± 0.43 dB per port as shown in Fig. 6(d). The discrepancy between the simulation and measured results is due to the dimension offset.

3.5. Mach–Zehnder interferometer

MZI is a prominent constituent of modulators[26,27], detectors[28], optical switches[29], filters[30], and sensors. In general, the MZI is mainly composed of two 3 dB couplers and phase-shifting arms. The MMI and directional coupler are the

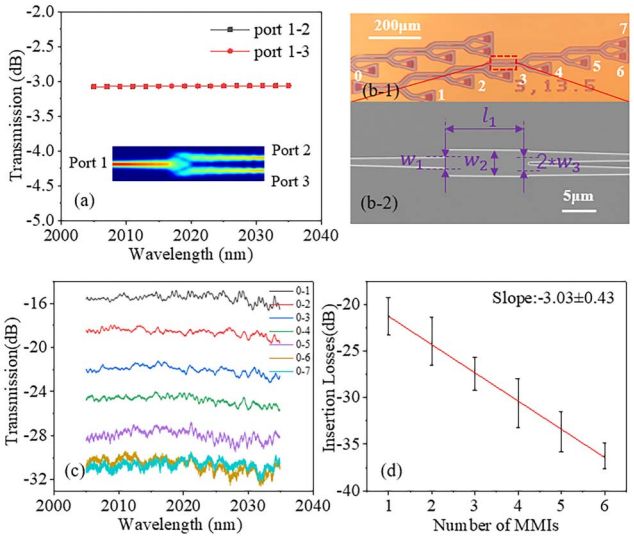

Fig. 6. (a) Simulated transmission spectrum of the 1 × 2 MMI at the wavelength of 2005–2035 nm. Inset: electric field distribution at the wavelength of 2020 nm. (b-1) Microscope view of cascaded 1 × 2 MMIs; the white numbers 0–7 represent the port number; (b-2) zoom-in SEM image of 1 × 2 MMI. (c) Measured transmission spectra of the 1 × 2 MMI at the wavelength of 2025 nm. (d) Total insertion losses as a function of the number of cascaded 1 × 2 MMIs at the wavelength range of 2020–2030 nm. The port numbers shown in (c) correspond to the number marked in (b-1), for example, the curve 0-1 shows the transmission spectrum from port 0 to 1.

commonly used 3 dB couplers. With higher fabrication tolerance, polarization independence, and wavelength independence, the MMI was used in our MZI structure. The radius of the bent waveguide inside the MZI was set to be 50 μm to avoid the bending loss. Here, we designed and fabricated the imbalanced MZI [Fig. 7(a)] with the 3 dB 1 × 2 MMI as discussed above. The length difference between the two asymmetric arms is 280 μm. Afterward, we measured the transmission spectra from port 1 to port 2. The insertion loss was less than 1 dB, and the extinction ratios of dips are larger than 20 dB, as shown in Fig. 7(b), which indicates the low insertion loss and balanced power splitting ratio of the MMI. The FSR of the MZI is 4.0 nm, and the corresponding group index is 3.66, which agrees well with the simulation results.

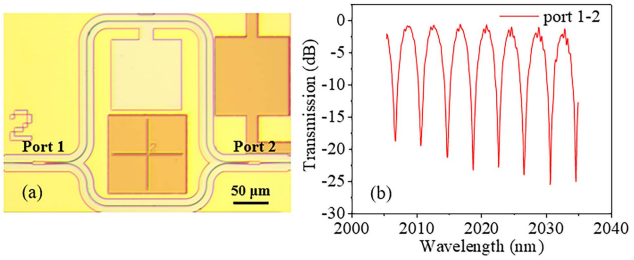

Fig. 7. (a) Optical image of the fabricated MZI. Ports 1 and 2 represent the input and output ports of the MZI. (b) Measured transmission spectrum of the MZI.

4. Conclusion

In summary, we have designed, fabricated, and characterized the fundamental passive silicon photonic components operating in the 2 μm waveband. All devices were etched by 150 nm on a 220 nm thick silicon layer in a silicon photonic MPW process. The propagation loss of the waveguide was 1.62 dB/cm, which was inferred from a ring resonator with an intrinsic quality factor as high as 3.0×10^5. The GC's coupling efficiency is about −7.9 dB. Waveguide crossings at this wavelength range were also fabricated for the first time, to the best of our knowledge, with an insertion loss of less than 0.08 dB. Finally, the MMI with a low insertion loss of −3.03 ± 0.43 dB was demonstrated in an imbalanced MZI with an extinction ratio larger than 20 dB. These low-loss passive devices could be critical functional units for on-chip optical interconnect and sensing applications at the 2 μm waveband.

Acknowledgement

This work was supported by the National Key Research and Development Program of China (No. 2019YFB2203003), National Natural Science Foundation of China (Nos. 91950204 and 61975179), Open Fund of the State Key Laboratory of Integrated Optoelectronics (No. IOSKL2020KF05), and Fundamental Research Funds for the Central Universities. We thank ZJU Micro-Nano Fabrication Center at Zhejiang University, and Westlake Center for Micro/Nano Fabrication, Instrumentation and Service Center for Physical Sciences at Westlake University for the facility support.

References

1. H. Sakr, T. D. Bradley, Y. Hong, G. T. Jasion, J. R. Hayes, H. Kim, I. A. Davidson, E. N. Fokoua, Y. Chen, K. R. H. Bottrill, N. Taengnoi, P. Petropoulos, D. J. Richardson, and F. Poletti, "Ultrawide bandwidth hollow core fiber for interband short reach data transmission," in *Optical Fiber Communication Conference Postdeadline Papers 2019* (2019), paper Th4A.1.
2. Z. Li, A. M. Heidt, J. M. Daniel, Y. Jung, S. U. Alam, and D. J. Richardson, "Thulium-doped fiber amplifier for optical communications at 2 μm," Opt. Express **21**, 9289 (2013).
3. M. N. Petrovich, F. Poletti, J. P. Wooler, A. M. Heidt, N. K. Baddela, Z. Li, D. R. Gray, R. Slavik, F. Parmigiani, N. V. Wheeler, J. R. Hayes, E. Numkam, L. Gruner-Nielsen, B. Palsdottir, R. Phelan, B. Kelly, J. O'Carroll, M. Becker, N. MacSuibhne, J. Zhao, F. C. Gunning, A. D. Ellis, P. Petropoulos, S. U. Alam, and D. J. Richardson, "Demonstration of amplified data transmission at 2 μm in a low-loss wide bandwidth hollow core photonic bandgap fiber," Opt Express **21**, 28559 (2013).
4. A. Schliesser, N. Picqué, and T. W. Hänsch, "Mid-infrared frequency combs," Nat. Photon. **6**, 440 (2012).
5. M. C. Estevez, M. Alvarez, and L. M. Lechuga, "Integrated optical devices for lab-on-a-chip biosensing applications," Laser Photon. Rev. **6**, 463 (2012).
6. N. Li, E. S. Magden, Z. Su, N. Singh, A. Ruocco, M. Xin, M. Byrd, P. T. Callahan, J. D. B. Bradley, C. Baiocco, D. Vermeulen, and M. R. Watts, "Broadband 2-μm emission on silicon chips: monolithically integrated holmium lasers," Opt. Express **26**, 2220 (2018).
7. R. Wang, S. Sprengel, A. Vasiliev, G. Boehm, J. Van Campenhout, G. Lepage, P. Verheyen, R. Baets, M.-C. Amann, and G. Roelkens, "Widely tunable 2.3 μm III-V-on-silicon Vernier lasers for broadband spectroscopic sensing," Photon. Res. **6**, 858 (2018).

8. W. Cao, D. Hagan, D. J. Thomson, M. Nedeljkovic, C. G. Littlejohns, A. Knights, S.-U. Alam, J. Wang, F. Gardes, W. Zhang, S. Liu, K. Li, M. S. Rouifed, G. Xin, W. Wang, H. Wang, G. T. Reed, and G. Z. Mashanovich, "High-speed silicon modulators for the 2 μm wavelength band," Optica **5**, 1055 (2018).
9. X. Wang, W. Shen, W. Li, Y. Liu, Y. Yao, J. Du, Q. Song, and K. Xu, "High-speed silicon photonic Mach–Zehnder modulator at 2 μm," Photon. Res. **9**, 535 (2021).
10. J. J. Ackert, D. J. Thomson, L. Shen, A. C. Peacock, P. E. Jessop, G. T. Reed, G. Z. Mashanovich, and A. P. Knights, "High-speed detection at two micrometres with monolithic silicon photodiodes," Nat. Photon. **9**, 393 (2015).
11. E. Ryckeboer, A. Gassenq, M. Muneeb, N. Hattasan, S. Pathak, L. Cerutti, J. B. Rodriguez, E. Tournie, W. Bogaerts, R. Baets, and G. Roelkens, "Silicon-on-insulator spectrometers with integrated GaInAsSb photodiodes for wide-band spectroscopy from 1510 to 2300 nm," Opt. Express **21**, 6101 (2013).
12. S. Zlatanovic, J. S. Park, S. Moro, J. M. C. Boggio, I. B. Divliansky, N. Alic, S. Mookherjea, and S. Radic, "Mid-infrared wavelength conversion in silicon waveguides using ultracompact telecom-band-derived pump source," Nat. Photon. **4**, 561 (2010).
13. X. Liu, B. Kuyken, G. Roelkens, R. Baets, R. M. Osgood, and W. M. J. Green, "Bridging the mid-infrared-to-telecom gap with silicon nanophotonic spectral translation," Nat. Photon. **6**, 667 (2012).
14. H. Subbaraman, X. Xu, A. Hosseini, X. Zhang, Y. Zhang, D. Kwong, and R. T. Chen, "Recent advances in silicon-based passive and active optical interconnects," Opt. Express **23**, 2487 (2015).
15. N. Hattasan, B. Kuyken, F. Leo, E. M. P. Ryckeboer, D. Vermeulen, and G. Roelkens, "High-efficiency SOI fiber-to-chip grating couplers and low-loss waveguides for the short-wave infrared," IEEE Photon. Technol. Lett. **24**, 1536 (2012).
16. J. Kang, Z. Cheng, W. Zhou, T. H. Xiao, K. L. Gopalakrisna, M. Takenaka, H. K. Tsang, and K. Goda, "Focusing subwavelength grating coupler for mid-infrared suspended membrane germanium waveguides," Opt. Lett. **42**, 2094 (2017).
17. J. Li, Y. Liu, Y. Meng, K. Xu, J. Du, F. Wang, Z. He, and Q. Song, "2-μm wavelength grating coupler, bent waveguide, and tunable microring on silicon photonic MPW," IEEE Photon. Technol. Lett. **30**, 471 (2018).
18. H. Xie, Y. Liu, W. Sun, Y. Wang, K. Xu, J. Du, Z. He, and Q. Song, "Inversely designed 1 × 4 power splitter with arbitrary ratios at 2-μm spectral band," IEEE Photon. J. **10**, 2700506 (2018).
19. E. J. Stanton, N. Volet, and J. E. Bowers, "Silicon arrayed waveguide gratings at 2.0-μm wavelength characterized with an on-chip resonator," Opt. Lett. **43**, 1135 (2018).
20. M. S. Rouifed, C. G. Littlejohns, G. X. Tina, H. Qiu, J. S. Penades, M. Nedeljkovic, Z. Zhang, C. Liu, D. J. Thomson, G. Z. Mashanovich, G. T. Reed, and H. Wang, "Ultra-compact MMI-based beam splitter demultiplexer for the NIR/MIR wavelengths of 1.55 μm and 2 μm," Opt. Express **25**, 10893 (2017).
21. S. Zheng, M. Huang, X. Cao, L. Wang, Z. Ruan, L. Shen, and J. Wang, "Silicon-based four-mode division multiplexing for chip-scale optical data transmission in the 2 μm waveband," Photon. Res. **7**, 1030 (2019).
22. L. Zhang, L. Jie, M. Zhang, Y. Wang, Y. Xie, Y. Shi, and D. Dai, "Ultrahigh-*Q* silicon racetrack resonators," Photon. Res. **8**, 684 (2020).
23. H. Liu, H. Tam, P. K. A. Wai, and E. Pun, "Low-loss waveguide crossing using a multimode interference structure," Opt. Commun. **241**, 99 (2004).
24. Y. Ma, Y. Zhang, S. Yang, A. Novack, R. Ding, A. E. Lim, G. Q. Lo, T. Baehr-Jones, and M. Hochberg, "Ultralow loss single layer submicron silicon waveguide crossing for SOI optical interconnect," Opt. Express **21**, 29374 (2013).
25. M. Johnson, M. G. Thompson, and D. Sahin, "Low-loss, low-crosstalk waveguide crossing for scalable integrated silicon photonics applications," Opt. Express **28**, 12498 (2020).
26. D. J. Thomson, F. Y. Gardes, J.-M. Fedeli, S. Zlatanovic, Y. Hu, B. P. P. Kuo, E. Myslivets, N. Alic, S. Radic, G. Z. Mashanovich, and G. T. Reed, "50-Gb/s silicon optical modulator," IEEE Photon. Technol. Lett. **24**, 234 (2012).
27. X. Tu, T. Y. Liow, J. Song, X. Luo, Q. Fang, M. Yu, and G. Q. Lo, "50-Gb/s silicon optical modulator with traveling-wave electrodes," Opt. Express **21**, 12776 (2013).
28. N. Youngblood, Y. Anugrah, R. Ma, S. J. Koester, and M. Li, "Multifunctional graphene optical modulator and photodetector integrated on silicon waveguides," Nano Lett. **14**, 2741 (2014).
29. Y. Shoji, K. Kintaka, S. Suda, H. Kawashima, T. Hasama, and H. Ishikawa, "Low-crosstalk 2 × 2 thermo-optic switch with silicon wire waveguides," Opt. Express **18**, 9071 (2010).
30. Y. Ding, M. Pu, L. Liu, J. Xu, C. Peucheret, X. Zhang, D. Huang, and H. Ou, "Bandwidth and wavelength-tunable optical bandpass filter based on silicon microring-MZI structure," Opt. Express **19**, 6462 (2011).